View metadata, citation and similar papers at core.ac.uk
brought to you by CORE
provided by Mountain Scholar (Digital Collections of Colorado and Wyoming)

Plasmoid Ejection and Secondary Current Sheet Generation from Magnetic Reconnection in Laser-Plasma Interaction

Quan-Li Dong (董全力),[1,*] Shou-Jun Wang (王首钧),[1] Quan-Ming Lu (陆全明),[2] Can Huang (黄灿),[2] Da-Wei Yuan (袁大伟),[1] Xun Liu (刘勋),[1] Xiao-Xuan Lin (林晓宣),[1] Yu-Tong Li (李玉同),[1] Hui-Gang Wei (魏会冈),[3] Jia-Yong Zhong (仲佳勇),[3] Jian-Rong Shi (施建荣),[3] Shao-En Jiang (江少恩),[4] Yong-Kun Ding (丁永坤),[4] Bo-Bin Jiang (蒋柏彬),[4] Kai Du (杜凯),[4] Xian-Tu He (贺贤土),[5,6] M. Y. Yu (郁明阳),[6,7] C. S. Liu (刘全生),[8] Shui Wang (王水),[2] Yong-Jian Tang (唐永健),[4] Jian-Qiang Zhu (朱健强),[9] Gang Zhao (赵刚),[3] Zheng-Ming Sheng (盛政明),[1,10] and Jie Zhang (张杰)[1,10,†]

[1]*Beijing National Laboratory of Condensed Matter Physics, Institute of Physics, Chinese Academy of Sciences, Beijing 100080, China*
[2]*CAS Key Laboratory of Basic Plasma Physics, University of Science and Technology of China, Hefei, Anhui 230026, China*
[3]*Key Laboratory of Optical Astronomy, National Astronomical Observatories, Chinese Academy of Sciences, Beijing 100012, China*
[4]*Research Center for Laser Fusion, China Academy of Engineering Physics, Mianyang 621900, China*
[5]*Institute of Applied Physics and Computational Mathematics, Beijing 100094, China*
[6]*Institute for Fusion Theory and Simulation, Physics Department, Zhejiang University, Hangzhou 310027, China*
[7]*Institute for Theoretical Physics I, Ruhr University, D-44780 Bochum, Germany*
[8]*Department of Physics, University of Maryland, College Park, Maryland 20742, USA*
[9]*National Laboratory on High Power Lasers and Physics, Shanghai, 201800, China*
[10]*Key Laboratory for Laser Plasmas (MoE) and Department of Physics, Shanghai Jiao Tong University, Shanghai 200240, China*

(Received 20 July 2011; published 22 May 2012)

Reconnection of the self-generated magnetic fields in laser-plasma interaction was first investigated experimentally by Nilson *et al.* [Phys. Rev. Lett. **97**, 255001 (2006)] by shining two laser pulses a distance apart on a solid target layer. An elongated current sheet (CS) was observed in the plasma between the two laser spots. In order to more closely model magnetotail reconnection, here two side-by-side thin target layers, instead of a single one, are used. It is found that at one end of the elongated CS a fanlike electron outflow region including three well-collimated electron jets appears. The (> 1 MeV) tail of the jet energy distribution exhibits a power-law scaling. The enhanced electron acceleration is attributed to the intense inductive electric field in the narrow electron dominated reconnection region, as well as additional acceleration as they are trapped inside the rapidly moving plasmoid formed in and ejected from the CS. The ejection also induces a secondary CS.

DOI: 10.1103/PhysRevLett.108.215001 PACS numbers: 52.38.Fz, 52.30.−q, 52.35.Vd, 52.50.Jm

Magnetic reconnection (MR) in plasmas is associated with explosive conversion of magnetic energy into plasma kinetic and thermal energies. In the process, plasma is accelerated in and ejected from a thin region where reconnection takes place [1–5]. The reconnection rate obtained from the experiments and solar observations is often found to be larger than that predicted by the standard Sweet-Parker and related models [4–6] and has been attributed to various collisionless and higher-dimensional effects, including Hall current and turbulence [7–12]. It has also been shown that the reconnection rate is enhanced by the formation of secondary magnetic islands and plasmoid ejection from the region, which can be highly unstable if the Lundquist number $S > 10^4$ [13]. These theoretical predictions are consistent with *in situ* observation of a secondary magnetic island near the center of the ion diffusion region in the near Earth magnetotail [14]. It is well known that in laser-matter interaction megagauss magnetic fields can be generated through the barotropic ($\nabla n_e \times \nabla T_e$) mechanism [15,16]. Nilson *et al.* [17] were the first to use two approaching laser-created plasmas to model the reconnection geometry. Definitive proof of MR taking place is provided by the measurements of Nilson *et al.* [17] and Li *et al.* [18] on magnetic topology changes using the time-resolved proton deflection technique and by the observations of Nilson *et al.* [17] on the highly collimated bidirectional plasma jets 40° off the expected MR plane. In this Letter, we investigate the structure of collisionless reconnection of the self-generated magnetic fields generated in laser-target interaction produced plasmas by using two coplanar plane targets with a gap in between, so that the colliding magnetic fields and plasmas are not electrically preconnected. Three well-collimated energetic (MeV) electron jets, or elongated electron diffusion regions (EDRs), inside and along the edges of a fanlike plasma outflow from the thin current sheet (CS) are observed. The energy gain is attributed to electron acceleration by the intense local inductive electric fields as well as inside a fast

 © 2012 American Physical Society

propagating plasmoid ejected from the elongated CS during the MR. The plasmoid also modifies the local magnetic field as it moves forward, producing a secondary CS. Our results agree quite well with that from numerical simulations and *in situ* observations.

The experiments were performed at the SG-II laser facility. The general setup is similar to that in our earlier work [8]. Here, two 0.7 mm $\times$ 0.3 mm $\times$ 50 μm thin Al foils separated by 150–240 μm are juxtaposed in the same (vertical) plane. Two heater laser beams are simultaneously (within $\pm$25 ps) focused by $F = 3$ optics onto each foil. The focal spots, 400 ± 25 μm apart, have diameters $<$150 μm FWHM. The incident laser intensity at each spot is $\sim O(10^{15})$ W cm^{-2}, and the total laser energy on each target is $\sim$450 J. The main diagnostics for the density of the laser-produced plasma is a modified Nomarski interferometer of magnification 3.5. A 527 nm, 150 ps FWHM Gaussian probe laser beam is directed perpendicular to the target plane at suitable intervals with respect to the heater beams. A polarization imaging system is used to measure the self-emission profile of the plasma, and a combination of reflective and bandpass ($\lambda \sim 532 \pm 1$ nm) interference filters is used to limit the detectable emissions. Three pinhole cameras with magnification 10 are used to monitor the x-ray emission from the front, back, and side of the plasma. At the top front of the target plane, an adjustable-range rubidium-acid-phthalate crystal spectrometer of $\sim$60 μm spatial resolution is used to characterize the plasma composition.

Figures 1(a) and 1(b) show the interferometric images of the laser-generated plasma at $t = t_0$ and $t = t_0 + 1.0$ ns, respectively, where $t = t_0$ corresponds to the instant when the tail-side half maximum of the heater pulse reaches the target front. By symmetry, the MR region is centered in the gap between the laser spots [17,18]. Figure 1(c) shows the profile of linearly polarized 532 nm emission from the plasma, with the darkest shade representing the brightest emission. Figure 1(d) shows the *upper half* of the MR region as obtained from a particle-in-cell (PIC) simulation using the experimental parameters (details given below). The main features in Fig. 1(c) are sketched and identified in Fig. 1(e), where the solid (red) lines show the brightest emission regions. All the panels in Fig. 1 and the left panel in Fig. 2 show the MR, or the x-z plane, where x is along the two laser spots. By following an edge, marked F in Fig. 1(a), the local plasma advection velocity is determined to be $\sim$2000 km/s [10]. The CS region (from X1 to X2) between the two laser spots is of length $\sim$350 μm. Here are two characteristic regions: R1 points to a fanlike (with full-opening angle $2\theta_{\rm rec} < 40°$) region of irregular plasma motion, and R2 points to a relatively calm and uniform plasma region. Figure 1(b) shows that after 1.0 ns the fanlike region has expanded and the jets lengthened. In the emission image in Fig. 1(c), one can clearly see the two bright (solid) lines marking the edges of the magnetic-separatrix region [see also Fig. 1(e)]. At the center of the fanlike region, a third bright line corresponding to a well-collimated energetic-electron jet appears. The three electron jets have similar widths ($\sim$ 55 μm) in the optical images. The variance of the lengths of the three jets in the time-resolved interferometric images indicates that the center jet is much faster than that on the two edges of the outflow fan, which has a bulk velocity $v_{\rm cf} > 600$ km/s, and that the center part of the CS has lengthened. Similar jetlike electron outflows have been observed in the magnetosheath and the corresponding numerical simulations [19], as well as around the separatrices of the reconnection layer [20].

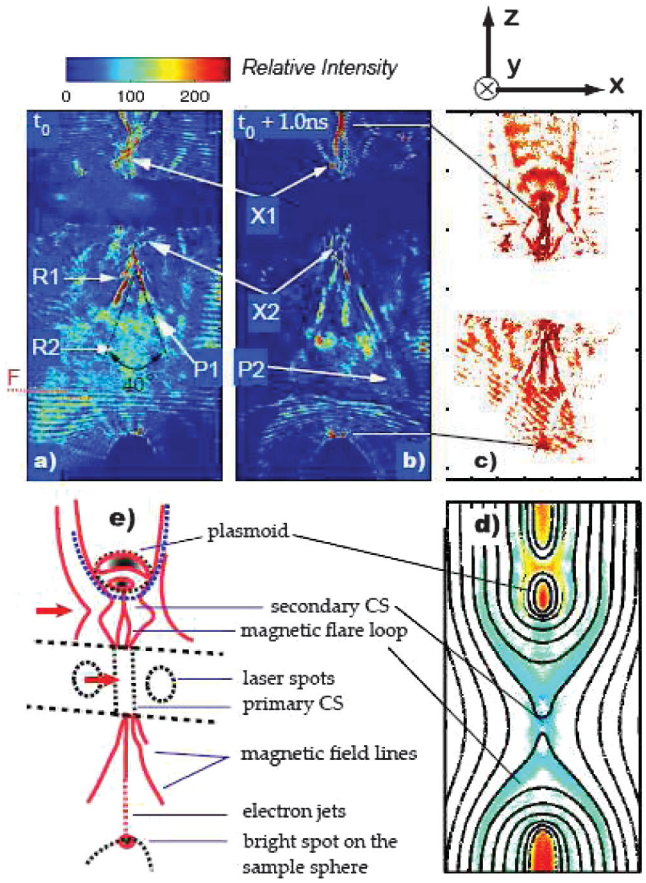

FIG. 1 (color). Interferometric image at $t = t_0$ ns (a) and $t = t_0 + 1$ ns (b), where t_0 is set at the half maximum of the laser-pulse tail. The electron diffusion region is between X1 and X2. F marks the edge of the advecting plasma. P1 and P2 (1.16 and 1.75 mm from X2, respectively) mark the location of a front of the expanding fanlike region at the two times, from which an outflow speed of $>$600 km/s is estimated. The angle of the fanlike plasma region is 35°–40°. (c) Linearly polarized self-emission image of the plasma. (d) PIC simulation result showing the current density, typical field lines, the secondary CS, and a plasmoid. (e) Schematic illustration of (c). The short thick (red) arrows indicate the plasma inflow directions for the primary and secondary CS.

The upper half of the MR region in Fig. 1 involves more complex behavior. There is also a fanlike outflow of plasma

from the CS. However, away from the primary CS there is a secondary CS with local MR. The secondary CS is connected to a flare loop at one end and a plasmoid at the other end, which in Fig. 1(e) is encircled by a thick black dashed line. Within the latter, one can see two bright areas (marked by red solid lines) that correspond to the leading and trailing ends of the plasmoid. One can also see that the trailing end of the plasmoid is connected to the secondary current sheet. A plasmoid can also be seen in the simulation result shown in Fig. 1(d). It is born inside the primary CS and grows rapidly. Its rapid ejection stretches the reconnected magnetic field lines, creating a secondary CS and MR. In Fig. 1(c) of the experimental results, the plasmoid's upward transport is manifested by its motion-blurred emission images. However, the generation process of the plasmoid needs further more detailed studies. These identifiable features in Fig. 1(c) are also marked in Fig. 1(e) and shall be discussed in more detail later. Our results thus support that of Shepherd and Cassak [21] and Uzdensky, Loureiro, and Schekochihin [22] and should be useful for analyzing abrupt solar and astrophysical events [23,24]. The top-bottom asymmetry of the MR region is inevitable in the case with plasmoid ejection, because the CS is highly unstable. Any small local disturbance can lead to rapid plasmoid ejection. That is, the ejection is stochastic, as proposed by Uzdensky, Loureiro, and Schekochihin [22].

More detailed characteristics of the primary CS are obtained from the x-ray images and the emission spectra. Figure 2 shows the x-ray pinhole image taken from the back of the Al targets. Intense x-ray emission comes from a narrow region of hot and dense plasma between the laser spots, while less intense x-ray emission comes from a fanlike region below it. The former region, of width ~85 μm, can be taken to be the ion diffusion region. A Ti wire of diameter 50 μm placed ~250 μm above and parallel to the target plane is used to determine the extent of the primary CS normal to the MR plane. As shown in Fig. 2, plasma ejection appears on the lower side without the Ti wire, but that on the upper side is mostly blocked by the latter. The extent of the CS is determined to be about 50 μm, indicating a quasi-two-dimensional (2D) nature of the MR region [19]. However, at longer times the plasma system becomes highly irregular and difficult to follow with our diagnostics. This may be due to the onset of transverse instabilities that lead to a strongly turbulent state [12]. The spatial distributions of the $K\alpha$ resonance lines (He-α lines) of the heliumlike Ti ions and their satellites, as shown in Fig. 3(a), are used to determine the cross-sectional size of the energetic-electron outflow [25]. Figure 3(b) shows the spatially integrated line spectra. Although the Ti wire is also in the transverse expansion paths of the two laser-produced Al plasmas, the He-α lines of Ti plasmas are present only in the midplane region (between 80 and 150 μm). Accordingly, together with the evidence given by the bright spot created by the central jet on the sampling sphere, as can be seen in the lower parts of Figs. 1(b), 1(c), and 1(e), one can conclude that a well-collimated energetic-electron jet is formed. The uniform continuum emission on both sides of the Ti He-α lines is from the Al plasma. Simulations by Shay *et al.* suggest that the structure of the fanlike MR plasma outflow and well-collimated energetic-electron jets can be attributed to competition and balance of the inductive electric field, the electron inertia, the Lorentz force, and divergence of the momentum flux [19]. However, more comprehensive

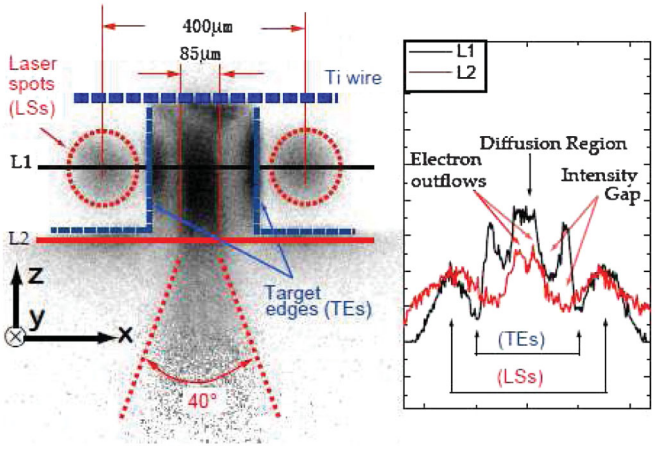

FIG. 2 (color). A typical x-ray pinhole image, with superimposed schematics of the experimental setup, and the corresponding intensity curves at two locations. The x-ray emission is strongest in the electron diffusion region at the center and is of width ~85 μm. The two central emission peaks in the L2 profile correspond to the two edge electron jets at the start of the fanlike region.

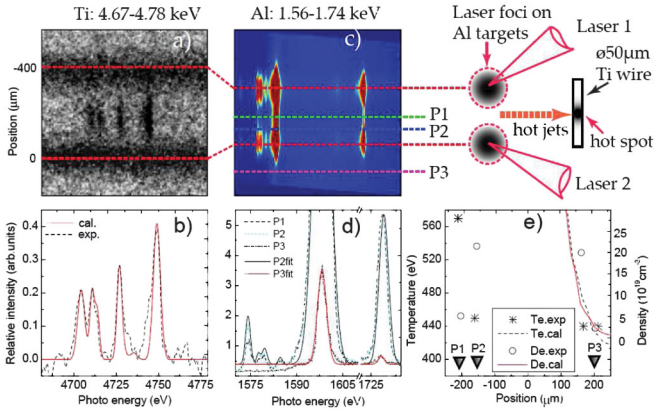

FIG. 3 (color). Spatially resolved emission of $K\alpha$ lines from heliumlike ions and the satellite lines from (a) the Ti wire and (c) the Al targets. (b) and (d) Typical line spectra from Ti and Al, respectively, together with the results calculated by using a nonlocal thermodynamic equilibrium model. (e) Local Al plasma electron density and temperature estimated from (d). The solid and dashed lines show the plasma electron density and temperature, respectively, obtained from a hydrodynamic code. The sketch shows the relevant experimental components.

laboratory and *in situ* magnetotail measurements are still needed in order to more definitively understand the detailed physics of the process [19,20].

Figure 3(c) shows simultaneously the measured He-α and Ly-α line emissions of the Al plasma, and Fig. 3(d) shows the space-resolved line spectra. The x-ray spectra of the Al plasma at the free-expansion edge, namely, along P3 in Fig. 3(c), shows a clear He-α line and a weak Ly-α line. From nonlocal thermodynamic equilibrium calculations, we found that this plasma region has temperature $\sim$440 eV and density $\sim 2.5 \times 10^{19}$ cm^{-3}, which are consistent with the interferometric measurements. The x-ray spectra from the plasma at the center, namely, along P1 in Fig. 3(c), clearly shows a saturated He-α line and a strong Ly-α line, as well as several satellite lines from Li-like ions, indicating an electron temperature of $\sim$570 eV and density of $\sim 4.8 \times 10^{19}$ cm^{-3}, the latter about double that at the free-expansion edge (i.e., along P3). Figure 3(e) shows the electron temperature and density from the experiments and hydrodynamic calculations. However, the Ti plasma produced by impact of the energetic jet electrons with the Ti wire has a temperature of $\sim 2300 \pm 100$ eV and density of $3.2 \pm 0.5 \times 10^{23}$ cm^{-3}, which are both considerably higher than that in the diffusion region. This is due to the fact that the collimated jet electrons have speeds much higher than the speed $\sim$600 km/s obtained from the intense linearly polarized 532 nm synchrotron radiation imaging of the plasma profile discussed above.

The electron and ion inertial lengths as calculated are $d_e = c/\omega_{\rm pe} = 0.77$–$1.06$ μm and $d_i = c/\omega_{\rm pi} \sim 54$–$75\,\mu$m, respectively, where c is the light speed and $\omega_{\rm pe}$ ($\omega_{\rm pi}$) is the electron (ion) plasma frequency. The electron density is $n_e \sim (2.5$–$4.8) \times 10^{19}$ cm^{-3}, and the average ionic charge is $Z \sim 10$. Accordingly, the width ~ 85 μm of the defined ion diffusion region in Fig. 2 is $\sim$1–1.5 times the ion inertial length. The widths of the EDRs are obtained by two methods, which are sensitive to the photon energy ranges. The pinhole x-ray image at >1.5 keV gives the widths of the EDRs as 7 and 15 μm as in Fig. 2, corresponding to $\sim(10$–$15)d_e$, respectively. On the other hand, the polarized emission image at 532 nm gives the widths of the three EDRs as ~ 55 μm. The difference in the EDR widths from the two measurement methods indicates that, as expected, the center regions of the EDRs are of higher temperature. The electron mean-free path is calculated as $\lambda_{e\rm MFP} \sim 114$ μm, which is larger than the measured current layer width. For the experimental parameters, we have the ratio between the ion skin depth and the Sweet-Parker width $d_i/d_{sp} \sim 10 > 1$, so that the Hall effect should be the main effect for the fast reconnection [26], and the binary collision is thus negligible in the CS, as also assumed for our PIC simulations. With detailed characteristics of the MR plasma region, and the separatrix magnetic field of $B_0 \sim 3.75$ MG inferred later, we now can the give the upper limit of the Alfvén speed as $V_A \sim 720$ km/s. The measured velocity $\sim$600 km/s of the two side EDRs in Fig. 1 is near the calculated value of V_A. However, the central EDR that starts later than the two side ones has clearly a higher propagation speed (since it can almost catch up with the latter), perhaps super-Alfvénic as predicted by PIC simulations.

We have carried out 2D PIC simulations of the main MR region using parameters close to those of our experiments. However, a large ($m_i/m_e = 100$) electron mass and a relatively low ($c/V_A = 30$) light speed are used [27]. The initial state is a Harris current sheet of width d_i in a $L_x \times L_z = 12.8d_i \times 102.4d_i$ simulation box. A guide field $B_y \sim 0.2B_0$, where $B_0\hat{z}$ is the strength of the sheared magnetic field, is added to model the experimental magnetic topology. Initially, the plasma temperature is $T_{i0} = T_{e0} = 0.011 m_e c^2$, and the plasma beta is $\beta_0 = 0.2$. Figure 1(d) shows a simulated current density distribution j_y (color coded) in the upper half of the MR region, together with several typical field lines (black lines). Here one also finds a plasmoid, together with the deformed magnetic field lines and a secondary CS, as observed in the experiments. However, it should be noted that our simulation does not include the initial laser-plasma interaction stage, since that would be beyond our computational resources. In fact, it models only the thin central MR region, which should be qualitatively similar for most MRs [7], and the initial values of the plasma and field parameters have also been taken from the already evolving system in the experiment.

The energetic jet electrons from the diffusion region are also diagnosed by using a magnetic spectrometer [28]. The jet electron energy can reach MeVs and obeys a power-law (of index -6.5) scaling at the high-energy tail for electrons up to ~ 2 MeV (the limit of our measuring equipment). We have also estimated the energy of the relativistic electrons from the synchrotron radiation [see Fig. 1(c)]. For relativistic electrons gyrating in the MR and Hall magnetic fields, the maximum electron energy $\mathcal{E}_{\rm max}$ is related to the maximum measured wavelength $\lambda_{\rm max}$ of the linearly polarized synchrotron radiation by $\mathcal{E}_{\rm max} = m_e c^2 (2.5 \times 10^{-2}/\lambda_{\rm max} B_0)^{1/2}$, and the corresponding electron gyroradius is $r_g = 1.70 \times 10^3 \sqrt{(\mathcal{E}_{\rm max}/0.511)^2 - 1.0}/B_0$. Assuming that the width of the electron diffusion region is of the order of $r_g \sim 55$ μm, and the maximum wavelength is $\lambda_{\rm max} = 532$ nm, we obtain 5.2 MeV as the measured energy of the relativistic electrons and $B_0 \sim 375$ T as the strength of the reconnected magnetic field. Existing numerical simulation and analytical estimates indicate that electrons can be accelerated to ultrahigh energies by the electric fields produced in MR, which explains the good collimation of energetic electrons [27,29–31]. For electrons to achieve MeV energy in $\sim$100 ps [the tolerant time for Fig. 1(c) to prevent from being blurred by plasma expansion; also see [17,18]], the electric field strength should be $\sim 10^8$ V/m. According to Faraday's law, such a

reconnection electric field corresponds to the annihilation of several tens of Tesla of magnetic fields in ~0.1 ns, or a dimensionless reconnection rate [19] 0.1–0.3, which is consistent with the Hall MR rate $\sim \tan(\theta_{\rm rec}) \sim 0.25$–$0.35$ obtained from measuring the local magnetic exhaust wedge angle $2\theta_{\rm rec}$ in Fig. 1. The corresponding acceleration length should then be ~1 cm. That is, the preaccelerated electrons trapped by the rapidly moving plasmoid have bounced many times before they gain sufficient energy to escape [32]. Accordingly, the MR electric field and plasmoid trapping, accounting for the good collimation and the power-law scaling, respectively, are both responsible for the observed characteristics of the high-energy electrons.

In summary, two suitably juxtaposed Al foil targets are used to produce in the laser-generated plasma the configuration of MR in the presence of a guide field. It is found that in the MR a plasmoid is generated and ejected from the CS. As it rapidly propagates away, it deforms the reconnected magnetic field and generates a secondary CS as well as flare loops. The primary MR also involves fanlike plasma outflows, in which appear intense well-collimated electron jets containing MeV electrons. The results are consistent with the theoretical prediction of anomalous plasmoid generation by an unstable CS, often invoked to interpret solar flares. Simulations show that the guide field can indeed lead to the fast formation of the plasmoid and the secondary CS. The results here also demonstrate that suitably designed laser-plasma interactions can be effective and economical for laboratory modeling high-energy-density astronomical and astrophysical phenomena.

This work is jointly supported by the National Natural Science Foundation of China (Grants No. 11121504, No. 10835003, and No. 11074297), the CAS Project No. KJCX2-YWT01, and the National Basic Research Program of China (Grant No. 2008CB717806). We also thank the staff of the target manufacture group at Research Center for Laser Fusion and the staff of the National Laboratory on High Power Lasers and Physics for their help in the experiments.

*qldong@aphy.iphy.ac.cn
†jzhang1@sjtu.edu.cn

[1] E. N. Parker, J. Geophys. Res. **62**, 509 (1957).
[2] P. Sweet, in *Electromagnetic Phenomena in Cosmical Physics*, edited by B. Lehnert (Cambridge University Press, Cambridge, England, 1958), p. 123.
[3] S. Masuda, T. Kosugi, H. Hara, S. Tsuneta, and Y. Ogawara, Nature (London) **371**, 495 (1994); D. E. Innes, B. Inhester, W. I. Axford, and K. Wilhelm, Nature (London) **386**, 811 (1997).
[4] J. Birn and E. R. Priest, *Reconnection of Magnetic Fields: Magnetohydrodynamics and Collisionless Theory and Observations* (Cambridge University Press, Cambridge, England, 2007).
[5] M. Yamada, R. Kulsrud, and H. Ji, Rev. Mod. Phys. **82**, 603 (2010).
[6] H. Ji, S. Terry, M. Yamada, R. Kulsrud, A. Kuritsyn, and Y. Ren, Phys. Rev. Lett. **92**, 115001 (2004).
[7] Z. Ma and A. Bhattacharjee, Geophys. Res. Lett. **23**, 1673 (1996); J. Birn *et al.*, J. Geophys. Res. **106**, 3715 (2001); M. Shay, J. F. Drake, B. N. Rogers, and R. E. Denton, J. Geophys. Res. **106**, 3759 (2001); F. S. Mozer, S. D. Bale, and T. D. Phan, Phys. Rev. Lett. **89**, 015002 (2002); Y. Ren, M. Yamada, H. Ji, S. P. Gerhardt, and R. Kulsrud, Phys. Rev. Lett. **101**, 085003 (2008); P. Cassak, M. A. Shay, and J. F. Drake, Phys. Rev. Lett. **95**, 235002 (2005).
[8] J. Y. Zhong *et al.*, Nature Phys. **6**, 984 (2010).
[9] Yu. V. Khotyaintsev, A. Vaivads, M. André, M. Fujimoto, A. Retinò, and C. J. Owen, Phys. Rev. Lett. **105**, 165002 (2010).
[10] L. Willingale *et al.*, Phys. Rev. Lett. **105**, 095001 (2010).
[11] W. Fox, A. Bhattacharjee, and K. Germaschewski, Phys. Rev. Lett. **106**, 215003 (2011).
[12] G. Lapenta and L. Bettarini, Europhys. Lett. **93**, 65 001 (2011); W. Daughton, V. Roytershteyn, H. Karimabadi, L. Yin, B. J. Albright, B. Bergen, and K. J. Bowers, Nature Phys. **7**, 539 (2011).
[13] D. Biskamp, Phys. Fluids **29**, 1520 (1986); W. Daughton, V. Roytershteyn, B. J. Albright, H. Karimabadi, L. Yin, and K. J. Bowers, Phys. Rev. Lett. **103**, 065004 (2009); R. Samtaney, N. F. Loureiro, D. A. Uzdensky, A. A. Schekochihin, and S. C. Cowley, Phys. Rev. Lett. **103**, 105004 (2009).
[14] R. Wang, Q. Lu, A. Du, and S. Wang, Phys. Rev. Lett. **104**, 175003 (2010).
[15] J. A. Stamper, K. Papadopoulos, R. N. Sudan, S. O. Dean, E. A. McLean, and J. M. Dawson, Phys. Rev. Lett. **26**, 1012 (1971).
[16] M. Borghesi, A. J. MacKinnon, A. R. Bell, R. Gaillard, and O. Willi, Phys. Rev. Lett. **81**, 112 (1998); R. D. Petrasso *et al.*, Phys. Rev. Lett. **103**, 085001 (2009).
[17] P. M. Nilson *et al.*, Phys. Rev. Lett. **97**, 255001 (2006).
[18] C. K. Li, F. H. Séguin, J. A. Frenje, J. R. Rygg, R. D. Petrasso, R. P. J. Town, O. L. Landen, J. P. Knauer, and V. A. Smalyuk, Phys. Rev. Lett. **99**, 055001 (2007).
[19] M. A. Shay, J. F. Drake, and M. Swisdak, Phys. Rev. Lett. **99**, 155002 (2007); T. D. Phan, J. F. Drake, M. A. Shay, F. S. Mozer, and J. P. Eastwood, Phys. Rev. Lett. **99**, 255002 (2007); H. Karimabadi, W. Daughton, and J. Scudder, Geophys. Res. Lett. **34**, L13 104 (2007).
[20] F. S. Mozer, S. D. Bale, J. P. McFadden, and R. B. Torbert, Geophys. Res. Lett. **32**, L24 102 (2005).
[21] L. S. Shepherd and P. A. Cassak, Phys. Rev. Lett. **105**, 015004 (2010).
[22] D. A. Uzdensky, N. F. Loureiro, and A. A. Schekochihin, Phys. Rev. Lett. **105**, 235002 (2010).
[23] J. Lin, Y.-K. Ko, L. Sui, J. C. Raymond, G. A. Stenborg, Y. Jiang, S. Zhao, and S. Mancuso, Astrophys. J. **622**, 1251 (2005); M. Shimizu, K. Nishida, H. Takasaki, D. Shiota, T. Magara, and K. Shibata, Astrophys. J. **683**, L203 (2008).
[24] D. A. Uzdensky, Space Sci. Rev. **160**, 45 (2011).
[25] M. Oka, M. Fujimoto, T. K. M. Nakamura, I. Shinohara, and K.-I. Nishikawa, Phys. Rev. Lett. **101**, 205004 (2008).

[26] M. Yamada, Y. Ren, H. Ji, J. Breslau, S. Gerhardt, R. Kulsrud, and A. Kuritsyn, Phys. Plasmas **13**, 052119 (2006).
[27] X. R. Fu, Q. M. Lu, and S. Wang, Phys. Plasmas **13**, 012309 (2006).
[28] J. Zhang, Y. T. Li, Z. M. Sheng, Z. Y. Wei, Q. L. Dong, and X. Lu, Appl. Phys. B **80**, 957 (2005).
[29] J. F. Drake, M. A. Shay, W. Thongthai, and M. Swisdak, Phys. Rev. Lett. **94**, 095001 (2005).
[30] P. L. Pritchett, Geophys. Res. Lett. **33**, L13 104 (2006).
[31] J. F. Drake, M. Swisdak, H. Che, and M. A. Shay, Nature (London) **443**, 553 (2006).
[32] Y. Wang, F. S. Wei, X. S. Feng, S. H. Zhang, P. B. Zuo, and T. R. Sun, Phys. Rev. Lett. **105**, 195007 (2010).